Struct Multidisc Optim (2005) 30: 181–192
DOI 10.1007/s00158-004-0508-7

RESEARCH PAPER

A. Gersborg-Hansen · O. Sigmund · R.B. Haber

Topology optimization of channel flow problems

Received: 8 June 2004 / Revised manuscript received: 20 September 2004 / Published online: 2 June 2005

Abstract This paper describes a topology design method for simple two-dimensional flow problems. We consider steady, incompressible laminar viscous flows at low-to-moderate Reynolds numbers. This makes the flow problem nonlinear and hence a nontrivial extension of the work of Borrvall and Petersson (2003).Further, the inclusion of inertia effects significantly alters the physics, enabling solutions of new classes of optimization problems, such as velocity-driven switches, that are not addressed by the earlier method. Specifically, we determine optimal layouts of channel flows that extremize a cost function which measures either some local aspect of the velocity field or a global quantity, such as the rate of energy dissipation. We use the finite element method to model the flow, and we solve the optimization problem with a gradient-based math-programming algorithm that is driven by analytical sensitivities. Our target application is optimal layout design of channels in fluid network systems. Using concepts borrowed from topology optimization of compliant mechanisms in solid mechanics, we introduce a method for the synthesis of fluidic components, such as switches, diodes, etc.

Keywords Viscous flow · Topology optimization · Finite element method · Sensitivity analysis · FEMLAB

1 Introduction

Topology optimization involves a search for a design that optimizes the response of a continuum system subject to given loads and constraints; the structure's connectivity is not prescribed a priori and is allowed to evolve during the optimization process. The seminal paper on numerical methods for topology optimization is by Bendsøe and Kikuchi (1988); see also Bendsøe and Sigmund (2004) for an overview of the subject.

This paper is concerned with applications of topology optimization to two-dimensional layout design of channel flows at low-to-moderate Reynolds numbers (laminar flow conditions) using the lubrication approximation for the flow, see Panton (1996). In this model, the flow is contained between plates that define the upper and lower surfaces of the channel. The separation distance between the plates determines the smallest characteristic length scale for the problem. One application that fits this model is the design of microfluidic devices in 'lab-on-a-chip' systems, where the channels consist of cavities in layered structures manufactured by, for example, silicon and polymer microfabrication methods. The geometry of a typical channel is often consistent with the assumptions of the lubrication theory; that is, the channel width W must be significantly larger than the channel depth h, and the channel geometry must be essentially planar. For example, the microfluidic dye laser described in Helbo et al. (2003) contains planar channels that meet these requirements: $W = 1$ mm and $h = 10\,\mu$m. However, the square channel cross sections, the highly three-dimensional channel paths, and the chaotic advective flows of the passive mixing devices discussed in Beebe et al. (2001) are beyond the scope of our current implementation.

Shape optimization techniques have previously been applied to fluid mechanics applications, such as minimum-drag profile design in laminar flows; see for example, Pironneau (1974), Glowinski and Pironneau (1975), Mohammadi and Pironneau (2001), and Lund et al. (2003). The new results presented here are an extension of recent work by Borrvall and Petersson (2003) that treats topology optimization of Stokes flows under the assumption that inertia can be neglected. Their solid isotropic material with penalization (SIMP) procedure allows for changes in the connectivity of the fluid layout during the optimization process, a class of design changes that are not allowed in earlier methods

A. Gersborg-Hansen (✉)
Department of Mechanical Engineering, Solid Mechanics, Technical University of Denmark, DK-2800 Lyngby, Denmark
E-mail: agh@mek.dtu.dk
Department of Mathematics, Technical University of Denmark, DK-2800 Lyngby, Denmark

O. Sigmund
Department of Mechanical Engineering, Solid Mechanics, Technical University of Denmark, DK-2800 Lyngby, Denmark

R.B. Haber
Department of Theoretical & Applied Mechanics, University of Illinois at Urbana-Champaign, Urbana, IL61801-2983, USA

for shape optimization of fluid problems. Our formulation accounts for fluid inertia in the governing equations, consistent with the assumptions of the lubrication approximation, and this makes the response analysis problem nonlinear. This makes the present work a nontrivial extension of Borrvall and Petersson (2003) because a new physical effect is included in the modelling and because the nonlinearity increases the computational complexity. We also apply techniques used to design compliant mechanisms in solid mechanics (Ananthasuresh et al. 1994; Sigmund 1997) to synthesize channel layouts for fluidic components (switches, diodes, etc.). Some preliminary results from the work reported here were presented in Sigmund et al. (2003).

The SIMP method (see Zhou and Rozvany (1991), Bendsøe and Sigmund (1999, 2004)) is one of the most widely used numerical techniques for topology optimization; it has been applied to mechanism design (Pedersen et al. 2001; Bruns et al. 2002), micro-electro-mechanical systems (MEMS) (Sigmund 2001b,c; Pedersen 2001), extreme materials (Sigmund 2000), and, more recently, to wave propagation problems in mechanics, acoustics and optics (Sigmund and Jensen 2003; Jensen and Sigmund 2004). Beyond the academic research environment, the aeronautical and automotive industries have embraced topology optimization as a practical design tool (Yang et al. 2000; Hörnlein et al. 2001).

The plan of the paper is as follows. Section 2 formulates the governing equations for channel flow with a variable depth or plate-separation distance. The design model allows the separation distance to vary with position, between a near-zero value that approximates a solid zero-flow condition and a maximum value equal to the true channel depth that indicates an open fluidic channel. Section 3 presents a generic statement of the topology optimization problem with examples of specific cost and constraint functions. Section 4 covers various numerical implementation issues, while Sect. 5 presents results from several numerical examples. Discussions of our results and of possible applications appear in Sect. 6, and conclusions are presented in Sect. 7.

2 Channel flow with nonuniform plate separation

This section formulates a rescaled version of the steady-state Navier–Stokes equations for incompressible Newtonian fluids under the assumptions of the lubrication theory. In essence, this section extends the methods of Borrvall and Petersson (2003) to nonlinear fluid flow including the inertia term.

The flow is assumed to be parallel to the mid-plane of the channel, with a parabolic velocity distribution through the depth and vanishing velocity at the top and bottom surfaces. Our model uses a nonuniform separation field to interpolate between the response in solid regions with zero flow and the response in channels with unimpeded flow. We denote by $\overline{h}$ the plate separation (depth) of an open channel.

The lubrication approximation requires the separation field to vary slowly in the flow direction to ensure that the velocity field is everywhere parallel (or nearly so) to the channel's mid-plane. Our method does not impose this constraint explicitly. However, the optimal separation fields generated by our SIMP-style procedure do satisfy this requirement; strong gradients are always orthogonal to the flow.

We begin by considering a steady, unforced flow of an incompressible Newtonian fluid in three spatial dimensions. The governing equations in non-dimensional form are

$$\left.\begin{aligned} Re^* \left(\nabla \hat{\mathbf{u}}\right) \hat{\mathbf{u}} &= -\nabla \hat{p} + \nabla \cdot \left(\nabla \hat{\mathbf{u}} + (\nabla \hat{\mathbf{u}})^{\mathrm{T}}\right) \\ \nabla \cdot \hat{\mathbf{u}} &= 0 \end{aligned}\right\} \tag{1}$$

in which the Reynolds number Re^* is treated as a constant, and the state variables $\hat{\mathbf{u}}$ and $\hat{p}$ are the three-dimensional velocity and pressure fields, respectively. The Reynolds number is defined by $Re^* = \overline{u} L^* / \nu$, where $\overline{u} > 0$ is a velocity scale, L^* is a length scale, and the kinematic viscosity is defined by $\nu = \mu / \rho$, in which μ and ρ are the dynamic viscosity and the mass density. For the present case of channel flow, we assign $L^* = \frac{7}{6}\overline{h}$, in which the factor $\frac{7}{6}$ is chosen to simplify the rescaled equations below. Appropriate boundary conditions must be appended to system (1) and its variants below to define a meaningful boundary value problem.

We next apply the lubrication theory (see for example Borrvall and Petersson (2003)) to system (1) to obtain the two-dimensional channel flow model. We map the three-dimensional geometry onto a domain $\Omega = \omega \times [-\frac{h(x_1,x_2)}{2L}; \frac{h(x_1,x_2)}{2L}] \subset \mathbb{R}^3$ in which the mid-surface ω is parameterized by coordinates (x_1, x_2), $h(x_1, x_2)$ is a possibly nonuniform plate-separation distance, and L is the next smallest length scale to L^*, such that $\overline{h} \ll L$. In particular, L is the smallest length scale in the two-dimensional flow field. We renormalize the problem using the parabolic velocity profile of the lubrication theory, as depicted in Fig. 1 and given by

$$\hat{\mathbf{u}}(\mathbf{x}) = \xi\,(x_3)\,[u_1(x_1, x_2)\mathbf{e}_1 + u_2(x_1, x_2)\mathbf{e}_2] \tag{2}$$

in which u_1 and u_2 are the in-plane velocity component fields, and

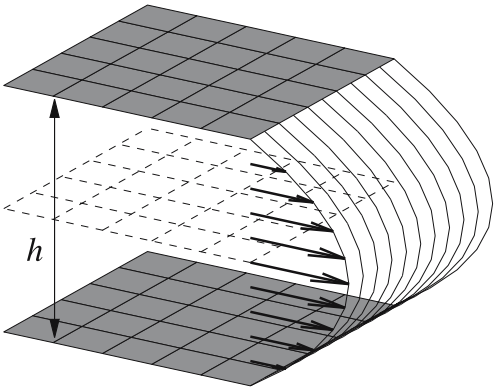

Fig. 1 The lubrication approximation. The plate-separation distance h is small relative to the plate dimensions. A two-dimensional velocity field, defined on the mid-plane surface (shown dashed), determines the three-dimensional flow field consistent with a parabolic distribution between the plates

$$\xi(x_3; x_1, x_2) = 1 - \left(\frac{2Lx_3}{h(x_1, x_2)}\right)^2. \tag{3}$$

The pressure field is assumed to be uniform in x_3 and is modelled by a scalar field on ω. We use this flow field representation to construct a Galerkin weighted residual statement for the governing equations (1); then we integrate to eliminate x_3 and localize the resulting two-dimensional weighted residual statement to obtain a rescaled system of governing equations on ω (see Gersborg-Hansen (2003), Borrvall and Petersson (2003) for details):

$$\left.\begin{aligned} Re\,(\nabla\mathbf{u})\,\mathbf{u} &= -\nabla p + \nabla\cdot\left(\nabla\mathbf{u} + (\nabla\mathbf{u})^{\mathrm{T}}\right) - \kappa\mathbf{u} \\ \nabla\cdot\mathbf{u} &= 0 \end{aligned}\right\} \tag{4}$$

in which $Re = 6/7Re^* = \frac{\overline{u}\overline{h}}{\nu}$. The rescaled velocity $\mathbf{u}$ is a two-dimensional velocity field defined as the restriction of $\hat{\mathbf{u}}$ to ω, p is the rescaled pressure field, such that $\hat{p}|_\omega = \frac{4}{5}p$, and the coefficient κ is a scalar function on ω given by

$$\kappa(x_1, x_2) = 10\left(\frac{L}{h(x_1, x_2)}\right)^2. \tag{5}$$

We note that κ is controlled by the dimensionless length scale ratio, $\frac{L}{\overline{h}}$.

The rescaled equations (4) take the form of the two-dimensional Navier–Stokes equations on ω with an extra term that accounts for out-of-plane viscous forces. There are two independent control parameters: the rescaled Reynolds number Re determines the magnitude of the inertia forces relative to the viscous forces, and the coefficient κ determines the magnitude of the out-of-plane viscous forces. In the case of Stokes flow $Re = 0$ the equations (4) are identical to a coupled-viscous flow problem, see Reddy and Gartling (2001). For the case $Re > 0$, the inertia term is nonstandard in the porous part of the domain. However, the underlying design problem only involves flow in the nonporous part of the domain; the porous region is merely an algorithmic device to implement a continuous transition between the limiting cases of viscous flow and zero flow. Therefore, we do not propose, and are not concerned with, any physical interpretation of the flow model in the transitional porous region.

The lubrication approximation is traditionally used for flows with low Reynolds numbers, where inertial effects are small, the flow is laminar, and system (1) is well posed. In the examples presented in Sect. 5, we restrict our attention to the range, $0 \le Re < 1000$. The flow is laminar and the stability of the solution is not a concern throughout this range.[1] For macroscopic applications, the upper end of this range corresponds to a low velocity or a more viscous fluid, such as an oil. However, smaller Reynolds numbers are typical for microfluidic flows of water-like fluids, with values $Re < 100$ (see Beebe et al. (2001), Helbo et al. (2003), Stroock et al. (2002)).

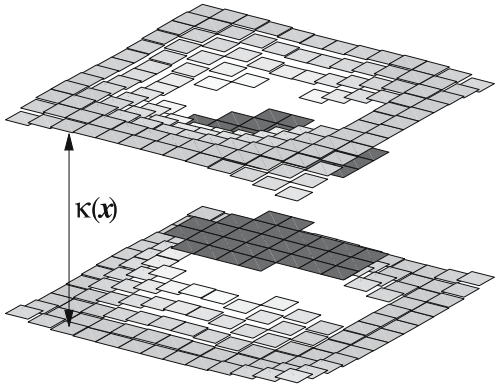

Fig. 2 The topology field $\kappa(\mathbf{x})$ scales an absorption term in a renormalized, two-dimensional version of the Navier–Stokes equations for the lubrication approximation (Fig. 1). It can also be interpreted as an inverse permeability coefficient; large values indicate a nearly impermeable (solid) medium, while small values allow unimpeded viscous flow

The coefficient κ attains its smallest value in regions where h is largest, indicating unimpeded channel flow as depicted in Fig. 2. On the other hand, κ becomes very large in regions where h approaches zero; this forces near-zero flow, consistent with solid regions. We require $h \in [\underline{h}, \overline{h}]$, where $0 < \underline{h} \ll \overline{h}$, and $\overline{h}$ is the plate-separation distance for an open channel. The lower bound on h ensures that κ remains bounded. Thus, the separation distance h is a suitable control for topology optimization that interpolates between the zero-flow conditions for a solid region and the conditions for unrestricted channel flow.

Alternatively, we can use the coefficient κ itself as the topology design field, where $\kappa \in [\underline{\kappa}, \overline{\kappa}]$. The lower bound $\underline{\kappa}$ corresponds to $\overline{h}$ according to (5), and we require $\overline{\kappa} \gg \underline{\kappa}$. Thus, $\kappa = \underline{\kappa}$ indicates unimpeded channel flow, and $\kappa = \overline{\kappa}$ indicates a solid region with no flow. If we abandon all reference to channel flow, (4) is simply a Brinkman-type model of Darcy's law for flow of an incompressible viscous fluid through a porous medium, cf. Reddy and Gartling (2001). In this setting, $\kappa = 1/Da$ is interpreted as an absorption coefficient given by the inverse Darcy number (see Gartling et al. (1996), Reddy and Gartling (2001)). Our method can thus be extended to layout design of three-dimensional flows by applying (4) directly, without rescaling, to solve for the three-dimensional flow and topology design fields. We use κ as the topology design field from here on.

3 Formulation of the optimization problem

Our goal is to find optimal distributions within a two-dimensional domain of solid regions (where $\kappa = \overline{\kappa}$) and open regions with unrestricted channel flow (where $\kappa = \underline{\kappa}$). To accomplish this, we introduce a standard representation of the topology design field and define a generic optimization program that can be fitted to any given design problem by selecting specific cost and constraint functions. The next

[1] Plane Poiseuille flow (one-dimensional channel flow with a uniform plate-separation distance) stays laminar in physical experiments under 'engineering conditions' up to critical values of Re which range from 1000 to 8000, cf. Panton (1996), where the plate-separation distance h and an average velocity are the length and velocity scales used to determine Re.

section presents details of our finite element implementation of this design model.

3.1 Representation of the topology design field

We introduce a scalar field $\alpha : \omega \to [0; 1]$ and a scaling function $s : \mathbb{R} \to \mathbb{R}$ so that $\kappa = s(\alpha)$. The scaling function provides a means to introduce and control an implicit penalty against intermediate values of κ in our implementation of the SIMP method. It is important to suppress intermediate values in the final design, because only the extreme values have a meaningful physical interpretation. However, the inclusion of intermediate values of κ is important in the optimization process because it transforms the topology optimization program from an integer format to a more convenient continuous format. In this work, we adopt the scaling function proposed by Borrvall and Petersson (2003):

$$s(\alpha) = \overline{\kappa} + \left(\underline{\kappa} - \overline{\kappa}\right) \alpha \frac{1+q}{\alpha+q} \tag{6}$$

in which $q > 0$ is a parameter that controls the strength of the implicit penalty on intermediate values of κ. Clearly, $\alpha = 0$ corresponds to a solid region with nearly zero flow according to $\kappa = 10L^2/\underline{h}^2$ (maximum absorption), while $\alpha = 1$ corresponds to unrestricted channel flow with $\kappa = 10L^2/\overline{h}^2$ (minimum absorption). We choose the limiting absorption values to enforce a 'small' flow rate in solid regions while ensuring that the problem remains well posed (e.g. $100|\mathbf{u}|_{\overline{\kappa}} \leq \max_\omega |\mathbf{u}|$).

Our finite element model uses element-wise continuous basis functions η_i to build a discontinuous model for α

$$\alpha(\mathbf{x}) = \sum_{i=1}^{M} \eta_i(\mathbf{x})\alpha_i \tag{7}$$

where M is the dimension of the discrete design model. Each basis function has support over a single element, so the model admits discontinuities in α across element boundaries. The absorption field κ is obtained by combining (6) and (7). We use element-wise constant basis functions in our current implementation, so that M is equal to the number of elements.

Borrvall and Petersson (2003) conclude that linear scaling functions tend to deliver discrete '0–1' optimal designs. The scaling (6) approaches a linear function as $q \to \infty$, so large values of q generate designs dominated by the extreme values of κ, while smaller values of q generate smoother designs with more intermediate values of κ.

3.2 Optimization problem

Let the domain ω, the boundary conditions as well as the values of Re, h and L be given. Then a generic optimization problem is

$$\left.\begin{array}{l} \min\limits_{\boldsymbol{\alpha}} \; c \\ \text{s.t.} \quad \mathbf{r} = \mathbf{0}\,, \quad g_j \leq 0\,, \quad 0 \leq \alpha_i \leq 1 \end{array}\right\} \tag{8}$$

in which c is a cost function and $\mathbf{r}$ is a finite element residual vector for the state problem (4). The first set of inequalities involves problem-specific constraint functions g_j, and the second set introduces box constraints on the design variables.

The MMA math programming algorithm,[2] introduced in Svanberg (1987), solves the optimization problem (8) for a fixed value of the penalty parameter q in 100–3000 iterations. It requires the values of the cost function c, the constraints $\mathbf{g}$ and the design sensitivities $\frac{\mathrm{d}c}{\mathrm{d}\boldsymbol{\alpha}}$ and $\frac{\mathrm{d}\mathbf{g}}{\mathrm{d}\boldsymbol{\alpha}}$ as input, and delivers an optimal set of design parameters $\boldsymbol{\alpha}_i$ that satisfy the box constraints. We terminate MMA when $\max |\boldsymbol{\alpha}^{k+1} - \boldsymbol{\alpha}^k| < 10^{-3}$, where k is the iteration number. A continuation algorithm gradually increases the value of q from $\underline{q}$ to $\overline{q}$, invoking an optimization by MMA for each new value of q. The continuation procedure suppresses premature convergence to undesirable local minima, while ensuring that the final design reflects the full-strength penalty against intermediate values of κ. The continuation algorithm terminates after the optimization step if $q = \overline{q}$; otherwise, it increments q by a factor q_{inc} and restarts the optimization algorithm.

As discussed in Sect. 4, the design sensitivities are derived analytically using the adjoint method (cf. Vidal et al. (1991), Michaleris et al. (1994)). The sensitivity analysis follows the same lines as described in the literature, see Pedersen et al. (2001), Bendsøe and Sigmund (2004) for topology optimization of compliant mechanisms in solid mechanics with prescribed displacements.

Topology optimization often requires special techniques, such as filtering or perimeter constraints, to establish a minimum design length scale and thereby guarantee a well-posed optimization problem. Here we consider problems where the cost function is the rate of energy dissipation or where there are resource constraints on the rate of energy dissipation. Borrvall and Petersson (2003) showed that intricate designs with finer length scales tend to dissipate more energy and are, therefore, not favored in this class of optimization problems. Thus, the complexity of the optimal design is self-limiting, and we require no special techniques to obtain a well-posed problem.

3.3 Cost functions and constraints

This subsection introduces specific cost functions and constraints that are used in the numerical examples presented in Sect. 5.

3.3.1 A cost function for minimizing the rate of energy dissipation

This cost function is designed to determine the most energy-efficient design. We define the cost function as half the rate of energy loss from macroscopic to microscopic scales due to viscosity; it takes the dimensionless form

$$\phi = \frac{1}{2} \int_\omega \left[\underbrace{\nabla\mathbf{u} \cdot \left(\nabla\mathbf{u} + (\nabla\mathbf{u})^{\mathrm{T}}\right)}_{\mathrm{I}} + \underbrace{\kappa(\mathbf{x})\mathbf{u} \cdot \mathbf{u}}_{\mathrm{II}} \right] \mathrm{d}\mathbf{x} \tag{9}$$

[2] The MMA algorithm is the property of Krister Svanberg, KTH, Sweden. For academic purposes it is free of charge.

where $\mathbf{u}$ is the velocity solution from the state problem (4). Term I is half of the part of the dissipation function that is associated with the in-plane components of the stretching tensor (cf. Currie (2003)), while term II is half the part associated with the out-of-plane components. The latter part arises from the parabolic velocity profile in the lubrication theory (2). From an optimization perspective, term II links the cost function directly to the two-dimensional velocity field.

Using standard finite element matrix notation, with $\overline{\mathbf{u}}$ denoting the solution vector of velocity coefficients, the discrete form of (9) takes the form

$$\phi = \frac{1}{2}\overline{\mathbf{u}}^{\mathrm{T}}\mathbf{K}\overline{\mathbf{u}}\,, \tag{10a}$$

$$\mathbf{K} = \sum_{l=1}^{M}\int_{\omega_l}\left(\mathbf{B}^{\mathrm{T}}\mathbf{I}_0\mathbf{B} + \kappa(\mathbf{x})\mathbf{N}^{\mathrm{T}}\mathbf{N}\right)\mathrm{d}\mathbf{x}\,,\quad \mathbf{I}_0 = \begin{bmatrix} 2 & 0 & 0\\ 0 & 2 & 0\\ 0 & 0 & 1\end{bmatrix} \tag{10b}$$

where M is the number of elements in the mesh, and ω_l is the two-dimensional domain of element l. The matrix $\mathbf{B}$ transforms velocity parameters into components of the stretching (strain rate) tensor; it has the same form as the strain–displacement matrix in finite element formulations for solid mechanics applications. The matrix $\mathbf{N}$ is the standard shape function matrix for the velocity field, cf. Zienkiewicz and Taylor (2000).

3.3.2 A cost function for controlling the local velocity

This cost function is designed to optimize local properties of the velocity field; it is similar in concept to the cost functions introduced by Pedersen et al. (2001) and Bendsøe and Sigmund (2004) for the design of compliant mechanisms in solid mechanics. The design goal is to find a channel layout that maximizes the velocity component in a specified direction of interest (DOI) defined over a given line segment $\mathbf{l} \in \omega$. Since maximizing the velocity component in a given direction is equivalent to minimizing the component in the opposite direction, we define our cost function (to be minimized) so that it measures the velocity component in the $-\mathbf{m}$ direction, where $\mathbf{m}(\mathbf{x})$ is a function that delivers a unit vector in the DOI for all $\mathbf{x} \in \omega$. For a given line segment $\mathbf{l} \in \omega$ and for a specified function $\mathbf{m}(\mathbf{x})$ on ω, the cost function for controlling the local velocity is

$$\zeta = -\int_{\omega}\delta(\mathbf{x}-\mathbf{l})(\mathbf{m}(\mathbf{x})\cdot\mathbf{u})\mathrm{d}\mathbf{x} \tag{11}$$

where δ is the Dirac delta function. In the discrete setting, the cost function in (11) reduces to a linear combination of nodal velocity degrees of freedom

$$\zeta = \bar{\mathbf{l}}^{\mathrm{T}}\overline{\mathbf{u}} \tag{12}$$

where $\bar{\mathbf{l}}$ is a sparse vector whose nonzero values correspond to velocity basis functions whose support set has a nontrivial intersection with $\mathbf{l}$.

We extend the above notation to address multiple load cases, multiple line segments and multiple unit vector fields that indicate directions of interest. We write

$$\zeta^{ijk} = -\int_{\omega}\delta\left(\mathbf{x}-\mathbf{l}^i\right)\left(\mathbf{m}^j(\mathbf{x})\cdot\mathbf{u}^k\right)\mathrm{d}\mathbf{x} \tag{13}$$

where the multi-index ijk indicates the line, the unit vector field that defines the DOI, and the load case. The ranges of the individual indices are $i \in [1; NLI]$, $j \in [1; NUV]$ and $k \in [1; NLC]$, where NLI, NUV and NLC are the numbers of lines, unit vector fields and load cases, respectively.

3.3.3 A cost function for controlling local velocity with distinct goals for two load cases

This cost function enables the synthesis of fluid mechanisms that are optimized for more than one goal. We consider two load cases ($NLC = 2$), each with a distinct line ($NLI = 2$) and a distinct unit vector field ($NUV = 2$) for controlling different aspects of the flow field in each load case. The generic minimization problem (8) is transformed to a max − min problem by considering the cost function

$$\theta = -\left(\min_q z_q\right),\quad q = 1, 2 \tag{14}$$

where

$$z_1 = \zeta^{111},\, z_2 = \zeta^{222} \tag{15}$$

cf. (13).

3.3.4 Channel volume constraint

We introduce a constraint function g (cf. (8)) that requires the volume fraction of the design domain occupied by open channels to be less than some specified value f, where $f \in [0; 1]$. The condition $g \le 0$ in the optimization program (8) enforces a resource constraint on the total channel volume, as described in Borrvall and Petersson (2003). This constraint function takes the form

$$g = \frac{a_i\alpha_i}{fA} - 1 \Leftrightarrow a_i\alpha_i \le fA \tag{16}$$

in which a_i is the area of the ith element, and A is the total area of the design domain ω. We note that this constraint involves the design parameters α_i only, and does not depend on the response solution.

3.3.5 Constraint on the rate of energy dissipation

Here we define a constraint function g that limits the rate of energy dissipation due to viscous effects. We use this function to obtain energy-efficient designs in optimization problems where the cost function is not an energetic measure. The constraint function is given by

$$g = \frac{\phi}{f\phi^*} - 1 \Leftrightarrow \phi \le f\phi^* \tag{17}$$

where ϕ is the rate of viscous dissipation (cf. (9)), $f > 1$ is a given constant, and ϕ^* is a reference dissipation rate, defined as the rate of dissipation for unimpeded channel flow throughout the domain, i.e. $\alpha_i = 1 \Rightarrow \kappa(\mathbf{x}) = \underline{\kappa}$ $\forall \mathbf{x} \in \omega$.

4 Implementation

4.1 Sensitivity analysis

We perform an analytical sensitivity analysis of the discrete response using the adjoint method, see Vidal et al. (1991), Michaleris et al. (1994), Pedersen et al. (2001), and Bendsøe and Sigmund (2004). To simplify the notation, let $\mathbf{s}$ be a vector of state variables that contains the velocity and pressure degrees of freedom (dof), $\mathbf{s} = [\overline{\mathbf{u}}\ \overline{\mathbf{p}}]^{\mathrm{T}}$.

Following standard adjoint sensitivity analysis procedures, we calculate $\frac{\mathrm{d}c}{\mathrm{d}\boldsymbol{\alpha}}$ by introducing a vector of Lagrange multipliers $\boldsymbol{\lambda}$ and assume that the governing equations are satisfied for the current design and the current value of $\mathbf{s}$. That is, $\mathbf{r}(\mathbf{s}) = \mathbf{0}$ cf. (8), so that the Lagrangian function

$$\mathcal{L} = c + \boldsymbol{\lambda}^{\mathrm{T}}\mathbf{r} \tag{18}$$

equals the cost function c. Next, we take the derivative of $\mathcal{L}$ with respect to the design variables $\boldsymbol{\alpha}$ using our knowledge that $\mathbf{r} = \mathbf{0}$ and that $c = c(\mathbf{s}(\boldsymbol{\alpha}), \boldsymbol{\alpha})$ (cf. Sect. 3.3). We find

$$\frac{\mathrm{d}\mathcal{L}}{\mathrm{d}\boldsymbol{\alpha}} = \frac{\partial c}{\partial \boldsymbol{\alpha}} + \boldsymbol{\lambda}^{\mathrm{T}}\frac{\partial \mathbf{r}}{\partial \boldsymbol{\alpha}} + \left(\frac{\partial c}{\partial \mathbf{s}} + \boldsymbol{\lambda}^{\mathrm{T}}\frac{\partial \mathbf{r}}{\partial \mathbf{s}}\right)\frac{\mathrm{d}\mathbf{s}}{\mathrm{d}\boldsymbol{\alpha}} \tag{19}$$

The last term, involving the unknown response sensitivities, is eliminated by requiring $\boldsymbol{\lambda}$ to solve

$$\left(\frac{\partial \mathbf{r}}{\partial \mathbf{s}}\right)^{\mathrm{T}}\boldsymbol{\lambda} = -\left(\frac{\partial c}{\partial \mathbf{s}}\right)^{\mathrm{T}} \tag{20}$$

where $\frac{\partial \mathbf{r}}{\partial \mathbf{s}}$ is the Jacobian of the residual equation. Since the prescribed degrees of freedom cannot vary, only the free degrees of freedom can make a nonzero contribution to $\frac{\mathrm{d}c}{\mathrm{d}\boldsymbol{\alpha}}$. Therefore, (20) simplifies to

$$\left(\frac{\partial \mathbf{r}_F}{\partial \mathbf{s}_F}\right)^{\mathrm{T}}\boldsymbol{\lambda}_F = -\left(\frac{\partial c}{\partial \mathbf{s}_F}\right)^{\mathrm{T}} \tag{21}$$

where a subscript F denotes a free degree of freedom and

$$\frac{\mathrm{d}c}{\mathrm{d}\boldsymbol{\alpha}} = \frac{\partial c}{\partial \boldsymbol{\alpha}} + \boldsymbol{\lambda}_F^{\mathrm{T}}\frac{\partial \mathbf{r}_F}{\partial \boldsymbol{\alpha}}. \tag{22}$$

We used (22) to evaluate the sensitivities of the cost and constraint functions appearing in Sect. 3.3 and found them to be in good agreement with finite difference approximations for $Re > 0$. In addition, sensitivities of the cost function ϕ obtained with (22) were found to agree with the results reported in Borrvall and Petersson (2003) for the Stokes flow case, $Re = 0$.

4.2 Optimization algorithm and finite element implementation

Following the approach described in Sigmund (2001a), we programmed the optimization algorithm in MATLAB, using external calls to MMA routines to compute the design updates. We used FEMLAB 2.3[3], a high-level partial differential equation (PDE) package with a convenient interface to MATLAB, to program the finite element and sensitivity analysis routines. FEMLAB takes the strong form of the governing equations (4) as input, performs a symbolic linearization and uses a Newton method to solve the nonlinear problem and deliver an approximate solution.

We implemented a mixed finite element (FE) model, with two types of triangular Lagrange elements: an element with linear velocity and pressure interpolations ($u1p1$) and an element with a quadratic basis for velocity and a linear basis for pressure ($u2p1$). The $u1p1$ element is economical in that it has fewer degrees of freedom, however it is not an LBB-stable element (cf. Zienkiewicz and Taylor (2000)) and can produce spurious oscillations in the pressure field. These oscillations do not directly influence the optimal design, because our cost and constraint functions do not depend explicitly on the pressure. Nonetheless, the $u2p1$ element, which is LBB-stable, tended to produce better designs than the $u1p1$ element in the examples we considered.

Although the $u2p1$ elements are stable for uniform κ fields, another form of instability is observed with both element types when a nonuniform κ field is introduced on a refined mesh. These instabilities are clearly visible in the vorticity field $\mathfrak{W} = \nabla \times \mathbf{u}$, with large nonphysical values even for smoothly varying κ fields. Similar stability problems for porous–viscous flow simulations have been reported by Gartling et al. (1996). The authors believe that a linear interpolation of κ instead of the present discontinuous interpolation is needed in order to stabilize the FE problem. While a robust solution to this problem was not realized during this study, we were able to circumvent it by avoiding highly refined meshes in the numerical studies reported in the next section.

We require a partition of the system matrix, $\frac{\partial \mathbf{r}_F}{\partial \mathbf{s}_F}$, for the sensitivity analysis, cf. (21). We obtain this partition via the transformation, $\frac{\partial \mathbf{r}_F}{\partial \mathbf{s}_F} = \mathcal{N}^{\mathrm{T}}\frac{\partial \mathbf{r}}{\partial \mathbf{s}}\mathcal{N}$, in which $\mathcal{N}$ is a matrix that pulls out the free dofs (cf. the FEMLAB maual (2001)). The $\mathcal{N}$ matrix is readily available from the FEMLAB solver. We also require unassembled element matrices to implement a method similar to that described in Sigmund (2001a). Although FEMLAB does not provide a method for retrieving element matrices, we devised a method to extract them by assembling the global matrix on a special discontinuous mesh, with each element having private nodes, as described in Gersborg-Hansen (2003).

Next we review various selections for tuning parameters and data initialization. First, we initialize the design at the beginning of the optimization process according to $\boldsymbol{\alpha} = \mathbf{0}$. This neutral selection allows for the maximum nonlinear response, but it is usually an infeasible design. Hence, the first

[3] Marketed by COMSOL, Inc., Stockholm, Sweden. Web-link: www.comsol.com

iterations of the MMA algorithm are devoted to returning the design to the feasible domain.

The selection of appropriate bounds for the penalization parameter $q \in [\underline{q}; \overline{q}]$ is problem dependent. The value of $\underline{q}$ is chosen to make the optimization problem sufficiently convex that the MMA algorithm is easily able to find optimal solutions in the early stages of the continuation procedure. The value of $\overline{q}$ is set sufficiently large that the final design is dominated by extremal ('0–1') values of alpha, yet sufficiently small that the later designs remain optimal with respect to the cost function.

The larger the value of q_{inc} in the continuation procedure, the faster the optimization process achieves a '0–1' design, but there is also an increasing chance that the optimizer will converge to an undesirable local minimum. For a well-posed optimization problem, such as minimizing the rate of energy dissipation subject to a channel volume constraint, we obtained good results when we increased q in steps of $q_{inc} \sim 2$. Smaller values of q_{inc} yielded practically the same designs in terms of the cost function. Moreover, we restarted the MMA algorithm whenever q is incremented to avoid introducing artificial discontinuities into the MMA solution procedure.

The dimensionless length scale ratio $\overline{h}/L$ has a strong influence on the relative importance of the inertia forces.[4] Since $\overline{h}$ is generally fixed by the problem data, the smallest length scale L in the two-dimensional channel layout is a critical parameter. For example, L might be defined as a typical channel width. Unfortunately, L can be difficult to estimate because the channel layout is not known a priori. The boundary conditions for the examples in the following section include parts of the boundary where an inflow velocity profile is prescribed. We take the width l_{in} of these inflow boundaries as a reasonable estimate of the channel width, and set $L = l_{in}$.

5 Numerical examples

This section presents numerical examples that demonstrate the capabilities of the proposed design method. Table 1 presents abbreviations that we use to describe the finite element model and the boundary conditions for each example. We are particularly interested in studying the influence of inertia effects on the optimal designs. That is, we are interested in problems with larger values of Re (but not so large as to cause a loss of laminar flow), and smaller values of κ. To realize the latter goal, we prefer larger values of $\overline{h}/L$, however, we are constrained by the assumption in the lubrication theory that $\overline{h}/L \ll 1$. To emphasize the effects of inertia, we henceforth set $\overline{h}/L = 1/3 \Rightarrow \underline{\kappa} = 90$. Furthermore, we set $\overline{h}/\underline{h} = 100 \Rightarrow \overline{\kappa} = 10^4 \underline{\kappa}$.

[4] If we rescale the ω plane, for a fixed length scale ratio and a fixed fluid viscosity, we cannot maintain the same value of κ. This is in contrast to the Reynolds number, which can be maintained at a constant value via consistent rescaling of the characteristic velocity $\overline{u}$. Hence our solutions are specific to the given length scales, even for Stokes flow ($Re = 0$). If we had used a standard SIMP penalization based on a nonlinear interpolation of the viscous stress tensor, then this scaling effect would not be present.

Table 1 Abbreviations for finite element data and boundary conditions. **n** is a unit outward normal vector, and **s** is a vector tangent to the face under consideration

Name	Description
$u1p1$	Element with continuous linear interpolations for velocity and pressure.
$u2p1$	Element with continuous quadratic velocity and continuous linear pressure interpolations.
NE	Number of elements. NE equals the number of design variables in the optimization problem.
$NDOF$	Number of degrees of freedom.
Parabola	Parabolic velocity profile: $\mathbf{u} \cdot \mathbf{n} = 4s(s-1)$ where $s \in [0; 1]$ parameterizes the part of the boundary where the parabolic profile is specified.
$p = 0$	Free outflow boundary condition. The velocity is not prescribed, and the pressure is set to zero ($p = 0$).
Straight out	The pressure is set to zero ($p = 0$), and the tangential velocity component is set to zero ($\mathbf{u} \cdot \mathbf{s} = 0$).
No slip	$\mathbf{u} = \mathbf{0}$. Enforced on the boundary wherever none of the other conditions are enforced.
DOI	Direction of interest. The arrows point in the direction in which the velocity is to be maximized.

As the subsequent example shows, even in the case $\overline{h}/L = 1/3$ the inertia effect is very small for Reynolds numbers that are consistent with microfluidic devices. However, we also demonstrate that the inertia effects can significantly impact the optimal design in flows with data values comparable to those in Borrvall and Petersson (2003); i.e. $\kappa \in [10^{-4}; 10^4]$, even though these values are inconsistent with our channel flow model.

5.1 Design of a bend

We consider the design of a bend, similar to Borrvall and Petersson (2003). The design domain and boundary conditions are displayed in Fig. 3d. The cost function and constraint are taken to be the dissipation rate ϕ and a channel volume constraint of 25%,

$$c = \phi, \quad g = \frac{a_i \alpha_i}{0.25A} - 1, \quad A = \sum a_i = 25 \tag{23}$$

in which **a** is a vector of element areas. From Fig. 3 we see that the bend has sharp corners for Stokes flow, but the corners become rounder for a large Reynolds number in response to the growth of the inertia term, cf. Sigmund et al. (2003). For $Re = 50$ we see very little geometry change relative to the Stokes flow result. Hence, we conclude that microfluidic channels should be straight to minimize dissipation.

5.2 A fluid mechanism

We consider flow through a device with the goal of finding the channel layout that reverses the flow in the direction of

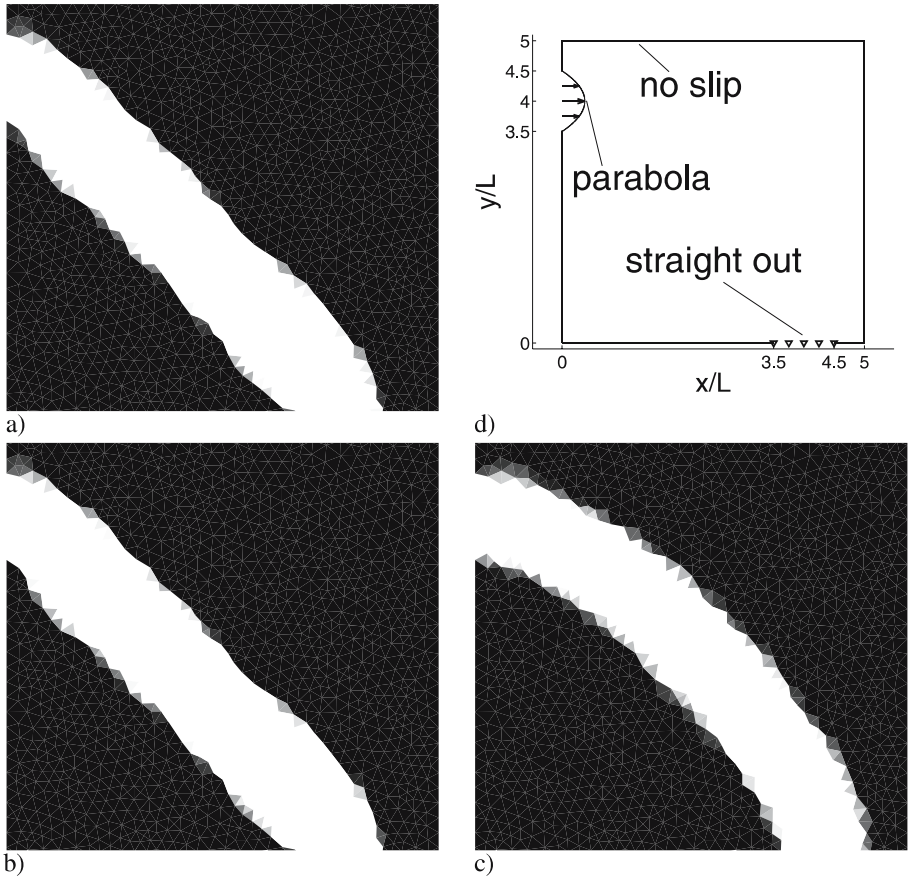

Fig. 3 Design of a bend. **a** Channel layout optimized at $Re = 0$, cost function $c = 1.296 \times 10^2$. **b** Channel layout optimized for $Re = 50$, cost function $c = 1.315 \times 10^2$. **c** Channel layout optimized at $Re = 850$, cost function $c = 1.559 \times 10^2$. **d** Design domain $\{(x, y) \in [0; 5] \times [0; 5]\}$ and boundary conditions {parabola ($x = 0$, $y \in [3.5; 4.5]$), straight-out ($x \in [3.5; 4.5]$, $y = 0$)}. $\kappa \in [90; 9 \times 10^5]$, final penalization value $q = 1.8 \times 10^{-3}$, $(q, q_{inc}) = (10^{-4}, 1.25)$, element $u1p1$, $NE = 2842$, $NDOF = 4440$. A large Reynolds number (larger than those associated with microfluidic devices) is required for inertia to have a significant effect on the design

interest (DOI) at the center of the device, cf. Fig. 4. For the cost function, we take a linear combination of the velocity degrees of freedom ζ, and we impose a constraint on the dissipation rate g_1 with a channel volume constraint g_2.

$$c = \zeta\,, \quad g_1 = \frac{\phi}{f\phi^*} - 1\,, \tag{24a}$$

$$g_2 = \frac{a_i \alpha_i}{0.6A} - 1\,, \quad f = \{5, 3\} \quad A = 5 \tag{24b}$$

In words, we maximize the velocity in the direction opposite to the input flow, with the dissipation rate limited to five or three times that of the undisturbed flow, while allowing channels to occupy up to 60% of the design domain. In this example, $\mathbf{m} = -\mathbf{e}_1$, cf. (11). The energy constraint ensures that the channel layout is energy efficient.

Our method successfully identifies channel layouts that reverse the flow in the center of the device, cf. Fig. 4c and 4e. As the limit on the dissipation rate is decreased, the channel design undergoes a topological change that could not have been obtained using standard shape optimization techniques starting from an ordinary channel design. For Stokes flow conditions, the work done by drag equals the energy dissipation rate, cf. Panton (1996), Pironneau (1974). Therefore, a channel with Stokes flow should always be straight to obtain minimum dissipation.

We do not have a true Stokes flow, due to the additional absorption term in the governing equations. However, this difference suggests a practical application for this design problem. Since, in practice, dissipation causes a pressure drop, it would be useful to generate designs that obey a limit on the energy dissipation rate. Such designs could be useful in microfluidic applications where there is a constraint on the allowed pressure drop, that might originate, for example, from flaws in the fabrication process.

We found that the $u2p1$ element was required to obtain a meaningful design in this example.

5.3 Fluid switch

This example uses $\underline{\kappa} = 10^{-4}$ hence it is inconsistent with the channel flow model and lacks a direct physical interpretation[5]. However it gives a 'proof of concept' for how a fluid

[5] The nonphysical value of κ was chosen since, despite many experiments, we were unable to obtain interesting results with physically meaningful channel dimensions.

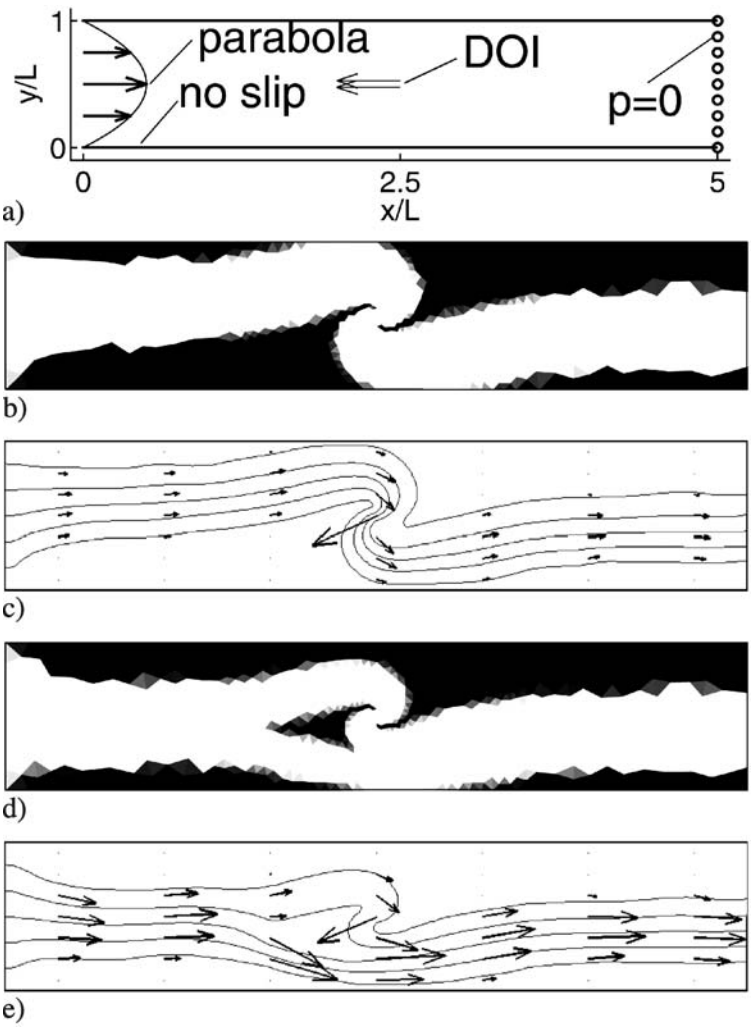

Fig. 4 Design of a fluid mechanism in Stokes flow. **a** Design domain $\{(x, y) \in [0; 5] \times [0; 1]\}$, DOI $(x = 2.5,\ y \in [0.475; 0.525])$ and boundary conditions $\{\text{parabola}\ (x = 0, y \in [0; 1]),\ p = 0(x = 5,\ y \in [0; 1])\}$. Reynolds number $Re = 0,\ \kappa \in [90; 9 \times 10^5]$, final penalization value $q = 3.2 \times 10^{-3},\ (q, q_{inc}) = (10^{-4}, 2)$, element $u2p1,\ NE = 1830$ and $NDOF = 8498$. **b** Channel layout optimized with dissipation fraction $f = 5$, **c** Flow field with streamlines for $f = 5,\ \min u_1(x = 2.5, y) = -6.66$. **d** Channel layout optimized with dissipation fraction $f = 3$ and **e** Flow field with streamlines for $f = 3,\ \min u_1(x = 2.5, y) = -1.82$. The flow rate in the solid regions (black) is small, but nonzero. Note that the length of the channel walls depends on the limit value in the dissipation constraint, cf. Fig. b and d

mechanism can be synthesized using the SIMP procedure. In the paragraphs below, we use the word 'fluid' to refer to a material that obeys (4) with $\kappa \in [10^{-4}; 10^4]$ (corresponding to $\overline{h}/L = 10^{2.5}$).

We consider the design of a fluid switch using two load cases. The design domain and boundary conditions are displayed in Fig. 5b. The goal is to design a switch that is activated by a change in the inflow velocity. The problem is formulated as follows: maximize the outflow rate across the line $\mathbf{l}^{\mathrm{A}}$ for a small inlet velocity (load case I), and maximize the outflow rate across the line $\mathbf{l}^{\mathrm{B}}$ for a larger inlet velocity (load case II). We use the inlet velocity as a characteristic velocity scale for the flow problem, hence this corresponds to an increase in the Reynolds number. In particular, we prescribe $Re = 0.5$ for load case I, and $Re = 50$ for load case II. We include a constraint g_1 on the dissipation rate to ensure an energy-efficient design (similar to the previous example) and we impose a channel volume constraint g_2 to ensure a channel-like layout. The cost function and constraints take the form

$$c = \theta\,,\quad g_1 = \frac{\phi}{10\phi^*} - 1\,,\quad g_2 = \frac{a_i \alpha_i}{0.5A} - 1\,,\quad A = 25 \tag{25}$$

where

$$z_1 = \zeta^{111} \quad \text{with} \quad \begin{cases} \mathbf{l}^1 = \mathbf{l}^{\mathrm{A}},\ \mathbf{m}^1 = -\mathbf{e}_2, \\ \mathbf{u}^1 = \mathbf{u}(Re = 0.5) \end{cases} \tag{26a}$$

$$z_2 = \zeta^{222} \quad \text{with} \quad \begin{cases} \mathbf{l}^2 = \mathbf{l}^{\mathrm{B}},\ \mathbf{m}^2 = \mathbf{e}_2, \\ \mathbf{u}^2 = \mathbf{u}(Re = 50) \end{cases} \tag{26b}$$

cf. (14) and (13).

The optimized fluid layout is shown in Fig. 5a. Figure 5c–f confirm that the flow rate is large across $\mathbf{l}^{\mathrm{A}}$ for load

Table 2 Switch performance. $\mathbf{u}^{(\cdot)} = \int\limits_{\mathbf{l}^{(\cdot)}} \mathbf{u} \cdot \mathbf{n} \mathrm{d}\mathbf{x}$

	Load case I ($Re = 0.5$)	Load case II ($Re = 50$)
Outflow at A, $\mathbf{u}^{\mathrm{A}}$	0.525	0.123
Outflow at B, $\mathbf{u}^{\mathrm{B}}$	0.126	0.525
Performance	$\frac{\int_{\mathbf{l}^{\mathrm{A}}} \mathbf{u}\cdot\mathbf{n}\mathrm{d}\mathbf{x}}{\int_{\mathbf{l}^{\mathrm{B}}} \mathbf{u}\cdot\mathbf{n}\mathrm{d}\mathbf{x}} = 4.17$	$\frac{\int_{\mathbf{l}^{\mathrm{B}}} \mathbf{u}\cdot\mathbf{n}\mathrm{d}\mathbf{x}}{\int_{\mathbf{l}^{\mathrm{A}}} \mathbf{u}\cdot\mathbf{n}\mathrm{d}\mathbf{x}} = 4.27$

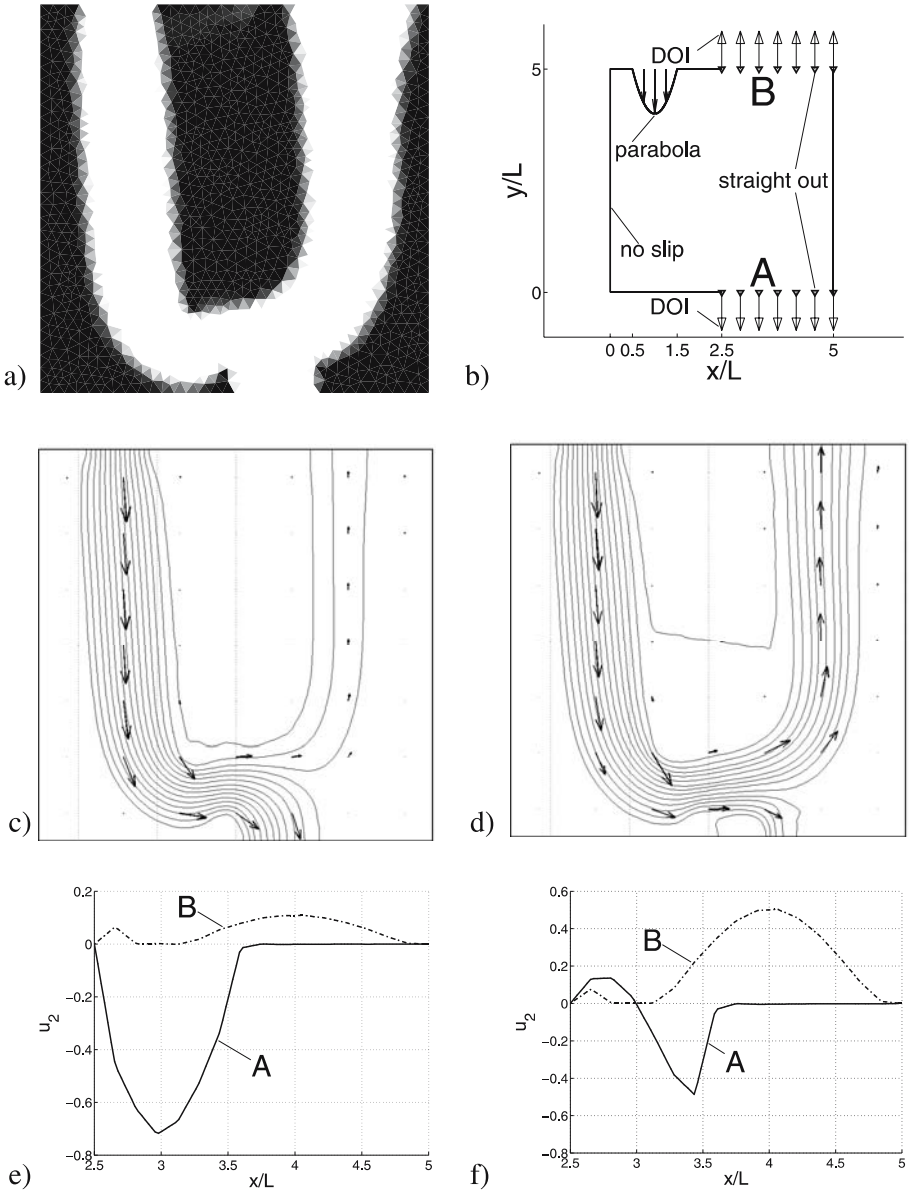

Fig. 5 Design of a switch using $\kappa \in [10^{-4}; 10^4]$ and two load cases. The channel layout is optimized for maximum outflow across outlet A for $Re = 0.5$ and for maximum outflow across outlet B for $Re = 50$, cf. Fig. b. **a** Optimized fluid layout, final penalization $q = 10^{-2}$, $(\underline{q}, q_{inc}) = (10^{-3}, 10)$, element $u1p1$ and $NE = 3153$, $NDOF = 4920$. **b** Design domain $\{(x, y) \in [0; 5] \times [0; 5]\}$, DOI $\{\mathbf{l}^{\mathrm{A}} = (x \in [2.5; 5], y = 0), \mathbf{l}^{\mathrm{B}} = (x \in [2.5; 5], y = 5)\}$ and boundary conditions {parabola ($x \in [0.5; 1.5], y = 5$) and straight out ($x \in [2.5; 5], y = \{0, 5\}$)}. **c** Velocity field for load case I. **d** Velocity field for load case II. **c**–**d** x-grid lines ':' at $x = \{0.5, 1.5, 2.5\}$. **e** Velocity profile along $\mathbf{l}^{\mathrm{A}}$ '$-$' and $\mathbf{l}^{\mathrm{B}}$ '$-\cdot-$' for load case I ($Re = 0.5$). **f** Velocity profile along $\mathbf{l}^{\mathrm{A}}$ '$-$' and $\mathbf{l}^{\mathrm{B}}$ '$-\cdot-$' for load case II ($Re = 50$). Note that recirculation occurs near outlet A for load case II, cf. Fig. d–f)

case I and large across $\mathbf{l}^{\mathrm{B}}$ for load case II. Note that the optimal design uses only part of $\mathbf{l}^{\mathrm{A}}$ for inflow in load case II, cf. Fig. 5f. The switch performance is quantified in Table 2, where we see that the final switch design alters the flow rates by a factor of four. Note that the channel volume constraint, in combination with the straight-out boundary condition, allows the optimization algorithm to determine the placement of the outflow boundary. This is similar to the optimal placement of supports in elastic design problems using the standard SIMP method, cf. Bendsøe and Sigmund (2004). The energy constraint ensures an energy-efficient (smooth) design, and it explains why only a part of the A boundary is used for outflow. Note also that this example could not have been done for pure Stokes flow since the inertia term is the key for obtaining the switching behavior.

6 Discussion

We used a prescribed parabolic velocity profile as a boundary condition in our numerical experiments to drive the flow. The parabolic profile is the solution to Poiseuille flow in a straight channel, but it is not the solution for the three-dimensional case. For this reason, it might be more realistic

to prescribe a pressure drop across the design domain in lieu of the parabolic profile. This alternative approach would simplify the sensitivity analysis, since the pressure would then enter as a boundary condition. The main drawback of such an approach is that it leaves the flow rate through the device to be determined a posteriori. In practice, the flow rate is usually prescribed in microfluidic experiments, cf. Helbo et al. (2003), as it is in this work.

The present SIMP method uses a raster-style design representation on a fixed mesh. This causes a rough description of the fluid–solid interface. Therefore postprocessing (shape optimization) of the results in this work is needed similar to postprocessing in all other applications of the topology optimization method.

6.1 Applications

The basic assumption in the lubrication approximation used is that the flow model remains two dimensional. Therefore the possible application areas are low-Reynolds-number channel-type layout problems e.g. for microfluidic channel-layout problems. For macro-size applications larger Reynolds numbers are easily obtainable hence inertia effects should be possible, however the lubrication approximation must remain valid. The latter may be hard to achieve since instabilities occur at low Reynolds numbers causing a transition from laminar to turbulent flow.

7 Conclusions

We have investigated the role of inertia in the topology optimization of channel flow problems. In keeping with the caveats of lubrication theory, we require the channel width to be much larger than the height. This constraint implies that inertia effects have negligible influence on the optimal channel layout in microfluidic devices where the flow is required to remain laminar and stable. Hence, the layout of microfluidic channels under these conditions is governed by the rule that the overall wall length should be minimized. This implies that the optimal design of a 90 degree bend has sharp corners.

On the other hand, our results show that inertia effects can be significant at somewhat larger (but still small) length scales that generate Reynolds number in the range $500 \leq Re \leq 1000$. In this case, we found optimal bends to be rounded.

For other channel geometries (e.g. comparable width-to-height ratios), it is necessary to do full three-dimensional modelling, and the conclusions might be different. We expect that the work reported here will provide a useful foundation for future work that uses fully three-dimensional modelling.

In order to obtain results that actually depend on inertia, we have also performed a number of experiments that violate the assumption of large width-to-height ratio. For these cases, we have designed mechanism-like fluidic devices that may act as flow inverters and flow switches.

Our implementation uses the commercial finite element code, FEMLAB 2.3, which is based on a MATLAB interface. We found this software to be very useful for our research, due to its focus on multiphysics problems, full access to system matrices and other finite element information, and the possibility of calling it as part of a MATLAB script. The main drawback is reduced computational performance relative to lower-level software development platforms.

Acknowledgement The authors thank Professor Robert D. Moser, Department of Theoretical and Applied Mechanics at University of Illinois at Urbana-Champaign (UIUC) and Professor Martin P. Bendsøe, Department of Mathematics at the Technical University of Denmark for helpful discussions. This work received financial support from Denmark's Technical Research Council (the "Phonon project") and from the Center for Process Simulation & Design at UIUC under grant number DMR 01-21695 from the United States National Science Foundation.

References

Ananthasuresh GK, Kota S, Kikuchi N (1994) Strategies for systematic synthesis of compliant MEMS. Dyn Syst Control 2:677-686

Beebe DJ, Adrian RJ et al. (2001) Passive mixing in microchannels: Fabrication and flow experiments. Mec Ind 2:343–348

Bendsøe MP, Kikuchi N (1988) Generating optimal topologies in structural design using a homogenization method. Comput Methods Appl Mech Eng 71(2):197–224

Bendsøe MP, Sigmund O (1999) Material interpolation schemes in topology optimization. Arch Appl Mech 69(9–10):635–654

Bendsøe MP, Sigmund O (2004) Topology optimization—theory, methods, and applications. Springer, Berlin Heidelberg New York

Borrvall T, Petersson J (2003) Topology optimization of fluids in Stokes flow. Int J Numer Methods Fluids 41:77–107

Bruns TE, Sigmund O, Tortorelli DA (2002) Numerical methods for the topology optimization of structures that exhibit snap-through. Int J Numer Methods Eng 55:1215–1237

COMSOL: FEMLAB Reference Manual for FEMLAB 2.3. COMSOL AB, Stockholm, www.comsol.se

Currie IG (2003) Fundamental mechanics of fluids. 3rd edn, Marcel Dekker, New York

Gartling DK, Hickox CE, Givler RC (1996) Simulation of coupled viscous and porous flow problems. Comput Fluid Dyn 7:23–48

Gersborg-Hansen A (2003) Topology optimization of incompressible Newtonian flows at moderate Reynolds numbers. Master's Thesis, Technical University of Denmark. Department of Mechanical Engineering Solid Mechanics, Lyngby

Glowinski R, Pironneau O (1975) On the numerical computation of the minimum-drag profile in laminar flow. J Fluid Mech 72:385–389

Helbo B, Kristensen A, Menon A (2003) A micro-cavity fluidic dye laser. J Micromech Microeng 13(2):307–311

Hörnlein HREM, Kocvara M, Werner R (2001) Material optimization: bridging the gap between conceptual and preliminary design. Aerosp Sci Technol 5(8):541–554

Jensen JS, Sigmund O (2004) Systematic design of photonic crystal structures using topology optimization: Low-loss waveguide bends. Appl Phy Lett 84(12):2022–2024

Lund E, Møller H, Jakobsen LA (2003) Shape design optimization of stationary fluid–structure interaction problems with large displacements and turbulence. Struct Multidisc Optim 25(5–6):383–392

Michaleris P, Tortorelli DA, Vidal C (1994) Tangent operators and design sensitivity formulations for transient non-linear coupled problems with applications in elastoplasticity. Int J Numer Methods Eng 37(14):2471–2499

Mohammadi B, Pironneau O (2001) Applied shape optimization for fluids. Oxford University, Oxford

Panton RL (1996) Incompressible flow. Wiley, New York
Pedersen CBW, Buhl T, Sigmund O (2001) Topology synthesis of large-displacement compliant mechanisms. Int J Numer Methods Eng 50(12):2683–2705
Pedersen NL (2001) On topology optimization of plates with prestress. Int J Numer Methods Eng 51(2):225–240
Pironneau O (1974) On optimum design in fluid mechanics. J Fluid Mech 64:97–110
Reddy JN, Gartling DK (2001) The finite element method in heat transfer and fluid dynamics, 2nd edn, CRC Press LLC, Boca Raton, Florida
Sigmund O (1997) On the design of compliant mechanisms using topology optimization. Mech Struct Machines 25(4):495–526
Sigmund O (2000) A new class of extremal composites. J Mech Phys Solid 48(2)397–428
Sigmund O (2001a) A 99 line topology optimization code written in MATLAB. Struct Multidisc Optim 21:120–127
Sigmund O (2001b) Design of multiphysics actuators using topology optimization—Part I: one-material structures. Comput Methods Appl Mech Eng 190(49–50):6577–6604
Sigmund O (2001c) Design of multiphysics actuators using topology optimization—Part II: two-material structures. Comput Methods Appl Mech Eng 190(49–50):6605–6627
Sigmund O, Gersborg-Hansen A, Haber RB (2003) Topology optimization for multiphysics problems: a future femlab application? In: Gregersen L (ed) Nordic Matlab Conference (held in Copenhagen), pp 237–242, Søborg, Denmark
Sigmund O, Jensen JS (2003) Systematic design of phononic band gap materials and structures by topology optimization. Philos Trans R Soc A: Math Phys Eng Sci 361:1001–1019
Stroock AD, Dertinger SKW, Ajdari A et al. (2002) Chaotic mixer for microchannels. Science 295:647–651
Svanberg K (1987) The method of moving asymptotes—a new method for structural optimization. Int J Numer Methods Eng 24:359–373
Vidal CA, Lee HS, Haber RB (1991) The consistent tangent operator for design sensitivity analysis of history-dependent response. Comput Sys Eng 2:509–523
Yang RJ, Chuang C-H, Che X, Soto CA (2000) New applications of topology optimization in automotive industry. Int J Vehicle Des 23(1):1–15
Zienkiewicz OC, Taylor RL (2000) The Finite Element Method (Parts 1–3). Butterworth Heinemann, Oxford
Zhou M, Rozvany GIN (1991) The COC algorithm, part II: topological, geometry and generalized shape optimization. Comput Methods Appl Mech Eng 89:197–224